

Substrate-induced strain in molybdenum disulfide grown by aerosol-assisted chemical vapor deposition

Lewis J Adams , Peter D Matthews , Juliana M Morbec 
and Nilanthy Balakrishnan* 

School of Chemical and Physical Sciences, Keele University, Keele ST5 5BG, United Kingdom

E-mail: n.balakrishnan@keele.ac.uk

Received 18 April 2024, revised 17 June 2024

Accepted for publication 2 July 2024

Published 11 July 2024



CrossMark

Abstract

Transition metal dichalcogenides have been extensively studied in recent years because of their fascinating optical, electrical, and catalytic properties. However, low-cost, scalable production remains a challenge. Aerosol-assisted chemical vapor deposition (AACVD) provides a new method for scalable thin film growth. In this study, we demonstrate the growth of molybdenum disulfide (MoS₂) thin films using AACVD method. This method proves its suitability for low-temperature growth of MoS₂ thin films on various substrates, such as glass, silicon dioxide, quartz, silicon, hexagonal boron nitride, and highly ordered pyrolytic graphite. The as-grown MoS₂ shows evidence of substrate-induced strain. The type of strain and the morphology of the as-grown MoS₂ highly depend on the growth substrate's surface roughness, crystallinity, and chemical reactivity. Moreover, the as-grown MoS₂ shows the presence of both direct and indirect band gaps, suitable for exploitation in future electronics and optoelectronics.

Supplementary material for this article is available [online](#)

Keywords: molybdenum disulfide, transition metal dichalcogenides, thin films, aerosol-assisted chemical vapor deposition, strain

1. Introduction

Molybdenum disulfide (MoS₂) has attracted tremendous attention owing to its two-dimensional layered structure and relatively large bandgap, which allows it to be used in electronics [1, 2], optoelectronics [3, 4], spintronics [5], gas and molecular sensing, and biomedical applications [6–9].

For device fabrication, the ability of bandgap tuning is a key lever of control [10]. This has previously been performed by various techniques including modulating the thickness of the material [11–13], doping [14–17], and strain engineering [18–23]. Strain is an important aspect of device technology due to its ability to induce changes in the electronic band structure of semiconducting materials [18]. In MoS₂ there are two ways to introduce strain: through external applied force or intrinsically *via* a targeted lattice constant mismatch between MoS₂ and the substrate. There is a substantial amount of work on extrinsic strain [19–23], but much less research has been conducted on substrate-induced strain on grown layers. The effect of lattice mismatch-induced strain in monolayer transition metal dichalcogenides is well documented [24], however,

* Author to whom any correspondence should be addressed.



Original content from this work may be used under the terms of the [Creative Commons Attribution 4.0 licence](#). Any further distribution of this work must maintain attribution to the author(s) and the title of the work, journal citation and DOI.

such strain cannot be negligible in multilayer systems. Strain in multilayers can become relaxed at a critical layer thickness by the introduction of misfit dislocations [25].

Traditional chemical vapor deposition (CVD) methods have been shown to produce high-quality monolayer to multilayer MoS₂ with triangular morphology. The morphology of the MoS₂ can be tuned by the growth temperature [26]. Such CVD methods involve high temperatures above 800 °C for the sulfurization of the molybdenum trioxide (MoO₃) precursor under high vacuum ($\sim 10^{-3}$ – 10^{-10} Torr) [27–29]. Thus, the CVD method is rather costly with the incorporation of multiple precursors, the use of high-temperature resistance quartz tubes and vacuum pumps. To reduce the cost of MoS₂ thin film production, exfoliation of bulk crystals has previously been studied but it has its own challenges. Sample qualities are often better than their CVD-grown counterparts, but their lateral sizes are limited to sub-micrometers, significantly smaller than the hundreds of microns size growth of the CVD method [30, 31].

It can be proposed that traditional CVD growth of MoS₂ has reached its zenith while non-traditional techniques, such as aerosol-assisted chemical vapor deposition (AACVD), have yet to be fully studied. AACVD is a solution-based growth method which involves the aerosolization of a solvent-based precursor to grow thin films. The aerosol-like nature of the precursor reduces growth temperature significantly [32, 33]. In addition, reducing the violating nature of the precursors potentially provides new avenues for high-quality large-scale cost-effective thin film production. However, due to the fast growth rate ranging from 10 s of nm min⁻¹ to 100 s of nm min⁻¹, it is difficult to control the layer thickness in the monolayer limit [34]. On the other hand, the role of substrates and their properties, such as lattice constants, crystallinity, surface roughness, and chemical reactivity on the AACVD growth process is yet to be explored.

In this work, we demonstrate the effect of substrate on the morphology of the as-grown MoS₂ thin films. Surface roughness, crystallinity, and chemical reactivity of the substrate and lattice mismatch between the substrate and MoS₂ played major roles in the morphology of the AACVD-grown MoS₂. The growth of 2H-MoS₂ was confirmed using a combination of elemental analysis, x-ray diffraction (XRD), and Raman and absorption spectroscopies. Raman spectroscopy and XRD are well-established characterization techniques that infer strain in semiconducting materials [20, 35, 36]. The experimental Raman modes were compared with computational results to confirm the type of strain induced on the AACVD-grown MoS₂ films. Moreover, the optical quality of our grown layers is comparable with the MoS₂ layers grown by the traditional high temperature CVD method. This study demonstrates the suitability of our low-cost AACVD method for the growth of high-quality MoS₂ thin films.

2. Experimental methods

Synthesis of tetrakis(diethyldithiocarbamato)molybdenum(IV) precursor: All reagents were purchased from Sigma–Aldrich and used without further purification.

The tetrakis(diethyldithiocarbamato)molybdenum(IV) [Mo(S₂CNEt₂)₄] precursor was synthesized using an adapted method previously reported by Decoster *et al* [37]. Molybdenum hexacarbonyl (1.0 g, 3.7 mmol, 1.0 equivalent) and tetraethyl thiuram disulfide (2.3 g, 7.4 mmol, 2.0 equivalent) were refluxed in acetone (40 ml) for 4 h at 80 °C. Then the reaction mixture was slowly cooled to room temperature. The reaction yielded a black/red microcrystalline solid, which was isolated by suction filtration and washed with hexane (3 × 30 ml) to provide the title product (1.5 g, 59%). The synthesized precursor was characterized by attenuated total reflection Fourier transform infrared (ATR-FTIR) spectroscopy, and XRD (see supporting information S1). Both ATR-FTIR and XRD spectra matched with previously reported literature [33, 38, 39].

Substrate preparation: Soda lime Glass, crystalline silicon (Si), Z-cut quartz, and silicon dioxide (SiO₂) were cut into 1 cm × 2 cm pieces. These substrates were ultrasonicated using acetone and isopropanol (5 minutes in each) and blow-dried with N₂ gas. Then further cleaned with oxygen plasma for 10 minutes using the HENNIKER's HPT-200 benchtop plasma system. Hexagonal Boron Nitride (hBN) crystal was purchased from hq⁺ graphene and exfoliated onto a SiO₂ substrate using the scotch tape method [40]. Highly Ordered Pyrolytic Graphite (HOPG) was purchased from Arger Scientific and cleaved into two pieces using a sharp sculpture blade. The freshly cleaved sides were used for MoS₂ deposition.

Aerosol-Assisted Chemical Vapor Deposition (AACVD): MoS₂ was deposited using a precursor molar concentration ranging from 0.145 to 0.290 mmol. The Mo(S₂CNEt₂)₄ precursor was dissolved in tetrahydrofuran (25 ml). The solution was suspended over a piezoelectric humidifier using a round bottom flask. Through the aerosolization process, an aerosol was produced and carried via a stream of N₂ gas (flow rate: 600 sccm) into a tube furnace, which contained the targeted growth substrate. The tube furnace was preheated to a temperature of 400 °C before the aerostation of the precursor. MoS₂ growth occurred for different durations spanning from 5 minutes to a maximum of 60 minutes. Once the time had elapsed, the furnace was slowly cooled down to room temperature under the nitrogen atmosphere. The growth temperature of 400 °C was selected *via* thermogravimetric analysis (TGA). Supporting information figure S1(c) shows the TGA profile of Mo(S₂CNEt₂)₄, which exhibited a four-step degradation profile similar to that previously reported by McCain *et al* [41]. For temperatures over 700 °C, similar to that of traditional CVD, a distribution of fine black dots was formed along the substrate surface. This is believed to be a result of the rapid decomposition of the tetrahydrofuran solvent used to produce the aerosol precursor preventing the aerosol from depositing on the substrate and nucleate to form crystals. Therefore, decomposition occurs in the gas phase resulting in widely spread fine individual carbon dots.

Optical studies: Optical images were taken using a Nikon Eclipse LV100ND optical microscope under brightfield imaging mode with magnification objectives of 5x, 10x, 20x, 50x,

and 100x. Raman spectra were measured using a DXR Thermo Scientific Raman microscope equipped with a 532 nm laser, a 50x objective and a 900 lines mm^{-1} grating. Ultraviolet-visible (UV-Vis) optical adsorption measurements were performed using a 50 Bio Varian UV-Vis spectrometer over a wavelength range of 200–800 nm. The surface-sensitive ATR-FTIR was performed using the Nicolet iS10 FTIR spectrometer equipped with a standard KBr beam splitter and DTGS detector in the frequency range of 4000–400 cm^{-1} .

Crystal structure, chemical and topographic characterization: XRD measurements were performed using a D8 Advanced powder diffractometer with a monochromatic $\text{Cu-K}\alpha$ radiation source of wavelength $\lambda = 1.5418 \text{ \AA}$ and an LYNXEYE XE (1D mode) detector for a 2θ range of 5° – 60° . X-ray photoelectron spectroscopy (XPS) was performed using an ESCA2SR spectrometer (ScientaOmicron GmbH) using monochromated Al $\text{K}\alpha$ radiation (1486.6 eV, 20 mA emission at 300 W, 1 mm spot size) with a base vacuum pressure of $\sim 1 \times 10^{-9}$ mbar. Charge neutralization was achieved using a low-energy electron flood source (FS40A, PreVac). Survey spectra were measured using 200 eV pass energy, and core levels with 50 eV pass energy. Binding energy scale calibration was performed using C–C in the C 1 s photoelectron peak at 284.8 eV. Analysis and curve fitting were performed using Voigt-approximation peaks using CasaXPS [42]. Scanning electron microscope (SEM) images and energy dispersive x-ray (EDX) spectra/maps were taken on both HITACHI TM4000Plus Tabletop Microscope and Zeiss Ultra Plus FEG SEM with an Oxford Instruments X-Max EDX detector using an accelerating voltage of 15 kV and 10 kV, respectively. Atomic force microscopy (AFM) images were acquired using a Park Systems FX40 Automatic AFM in tapping mode.

3. Results and discussion

The MoS_2 growth conditions were optimized by the deposition of MoS_2 thin films on glass (soda lime glass) substrates using a modified AACVD method. $\text{Mo}(\text{S}_2\text{CNEt}_2)_4$ was deployed as a single source precursor for the growth. The optimized growth temperature of $T = 400^\circ\text{C}$ is significantly lower than the traditional CVD growth. The morphology of the grown MoS_2 is altered by changing the precursor concentration, growth time and substrate position within the AACVD furnace. Nanorod-like structures were grown with a lateral size of $\sim 10 \mu\text{m}$ for a precursor concentration of 0.145 mmol, and a growth time of 5 minutes. Dendrite-like structures were obtained for a precursor concentration of 0.29 mmol and a growth time of 60 minutes. When the substrate moved closer to the aerosol injection site, continuous coverage of bulk configurations was obtained. Figure 1 shows the optical and AFM images of the grown structures on the glass substrate. This work focuses on the detailed study of MoS_2 growth obtained at a precursor concentration of 0.29 mmol, growth time of 60 minutes and growth temperature of 400°C .

The chemical composition of the MoS_2 grown on the glass substrate was assessed by EDX and XPS. Figure 2(a) shows

SEM backscattered electron image and EDX elemental maps of MoS_2 grown on the glass substrate. The EDX analysis shows the stoichiometric composition is $[\text{Mo}] = 20.3$ atomic % and $[\text{S}] = 42.0$ atomic %, which is close to $[\text{Mo}]: [\text{S}] = 1:2$ and confirmed no or very little oxidation (oxygen mainly coming from the glass substrate), see supporting information S2. In figure 2(b), the Mo 3d band of the XPS spectrum was fitted to two spin-orbit states $3d_{5/2}$ and $3d_{3/2}$ at binding energies of 228.9 and 232.5 eV, respectively. The XPS spectra indicated little to no MoO_3 inferring that the layers had not oxidized during the growth process due to the presence of the nitrogen atmosphere. Thus, the presence of little MoO_3 is due to passive surface oxidation after the growth. Analysis of the XPS spectrum yields a stoichiometric ratio of $[\text{Mo}]: [\text{S}] = 1:2$, consistent with the formation of MoS_2 . The broad S 2p singlet peak at 226.6 eV suggests the formation of the 2H-phase of MoS_2 [43, 44].

Figure 3 shows the UV-Vis spectrum of the MoS_2 dendrite-like structure grown on the glass substrate. The spectrum showed a strong (C) exciton peak at 415 nm and a weak (B) exciton peak at 613 nm. The B exciton peak at 613 nm is attributed to direct excitonic transition in the K point of the Brillouin zone and is a result of both interlayer and spin-orbit coupling. The C exciton peak at 415 nm is related to higher-level intra-band transitions from the P point of the Brillouin zone [45]. The A excitonic transition was not conclusively observed in the spectra. To determine the band gap, E_g , of the MoS_2 , Tauc plots were plotted using $(\alpha h\nu)^{\frac{1}{n}} = A(h\nu - E_g)$, where $h\nu$ is the incident photon energy, n is the exponent that reflects the type of electronic transition with values of 2 and $\frac{1}{2}$ refers to indirect and direct transition, respectively, A is a proportionality constant, and α is the absorption coefficient ($\alpha = 2.302 A/t \text{ cm}^{-1}$ and $t = 1.2 \mu\text{m}$ is the layer thickness) of MoS_2 [46, 47]. The MoS_2 exhibits an indirect bandgap of 1.5 eV and direct band gaps of 2.4 eV. The simultaneous presence of both types of band gap is an indicator of the presence of amorphous MoS_2 which corresponds to the particle-like droplets in the background witnessed in the SEM images, see supporting information S3. This dual-band gap has been reported to have promising photocatalytic properties for MoS_2 nanospheres [46]. The presence of dual-band gap in our as-grown MoS_2 could be suitable for wavelength tunable optoelectronic components.

To test the AACVD MoS_2 growth on different substrates, we chose HOPG, exfoliated hBN, Si, Z-cut quartz and SiO_2 . Figure 4 shows the schematic crystal structure of different substrates used for the growth. The six substrates are arranged by their microscopic surface roughness, which was determined by AFM height profiles. The average surface roughness (R_a) was quantified by taking the average of the root mean square roughness (S_q) and the arithmetic roughness (S_a) from the substrates' surface profiles (see supporting information S4 and table S1). The surface analysis showed that both HOPG and hBN are nearly atomically flat with R_a values of $73.4 \pm 8.8 \text{ pm}$ and $81.3 \pm 9.7 \text{ pm}$, respectively. On the other hand, quartz and SiO_2 showed the highest surface roughness of $1.8 \pm 0.4 \text{ nm}$ and $2.6 \pm 0.2 \text{ nm}$, respectively. The

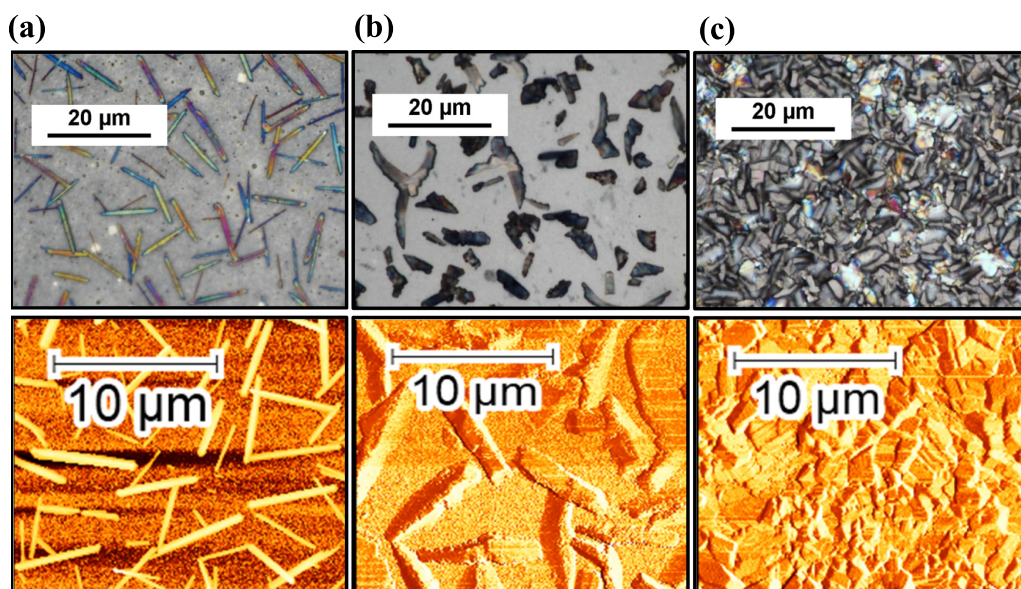


Figure 1. Optical (top) and AFM (bottom) images of MoS₂ structures grown on a glass substrate at various growth conditions. (a) Precursor concentration of 0.145 mmol for a growth time of 5 minutes. Precursor concentration of 0.290 mmol for a growth time of 60 minutes at the center of the heating zone (b) and closer to the aerosol injection site (c).

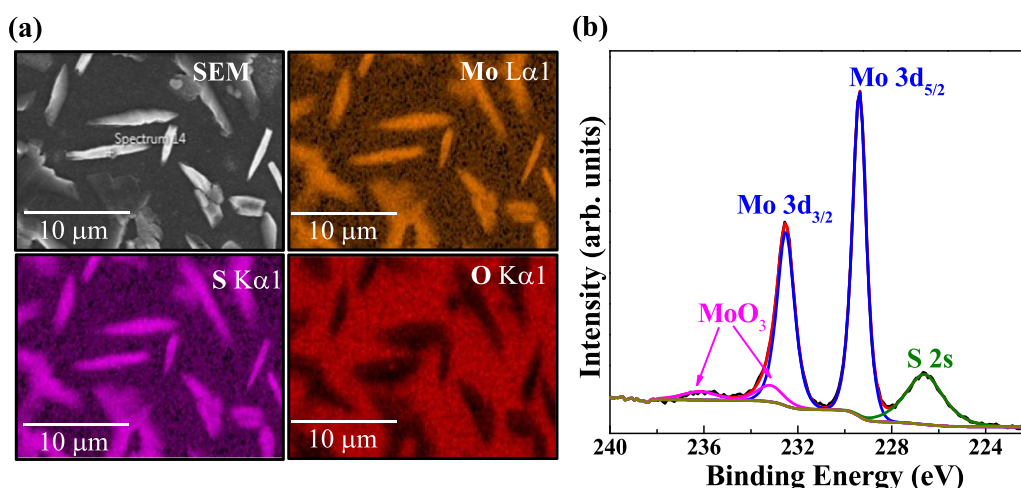


Figure 2. (a) SEM image and EDX map, and (b) XPS spectrum of dendrite-like structures grown on the glass substrate using a precursor concentration of 0.29 mmol, growth time of 60 minutes and growth temperature of 400 °C.

R_a values of Si and glass are intermediate with 399.7 ± 97.7 pm and 676.6 ± 53.3 pm, respectively. All the substrates have melting points over 900 °C which is considerably higher than the AACVD MoS₂ growth temperature of $T = 400$ °C. Thus, the surface roughness did not change during the growth process.

In addition, the chemical activity of the substrates follows the same trend except for glass. The soda lime glass is a penta-atomic system and the most chemically reactive substrate. SiO₂ is the second most chemically active substrate due to its dangling bonds while hBN is chemically inert due to its strong covalent boron-nitrogen bonds and wide band gap [48, 49]. Furthermore, the smoother substrates such as hBN and HOPG are highly crystalline compared to other substrates.

Particle-like morphology growth of MoS₂ was observed on hBN (see supporting information figure S5). This may be due to the poor adhesion between the precursor aerosol and chemically inert hBN. Consequently, decomposition of the precursor must occur in the gas phase causing evaporation, precipitation and thermolysis [47]. This resulted in the continuous coverage of MoS₂ nanoparticles on top of the exfoliated hBN flakes. The same growth morphology was observed on the Si substrate, which has a slightly higher surface roughness compared to hBN and is a little more chemically reactive due to its dangling Si bonds [50]. With increasing surface roughness, dense regions of branched particles were witnessed on quartz and dendrite-like crystalline structures were grown on the SiO₂. The increased surface roughness allows the absorption

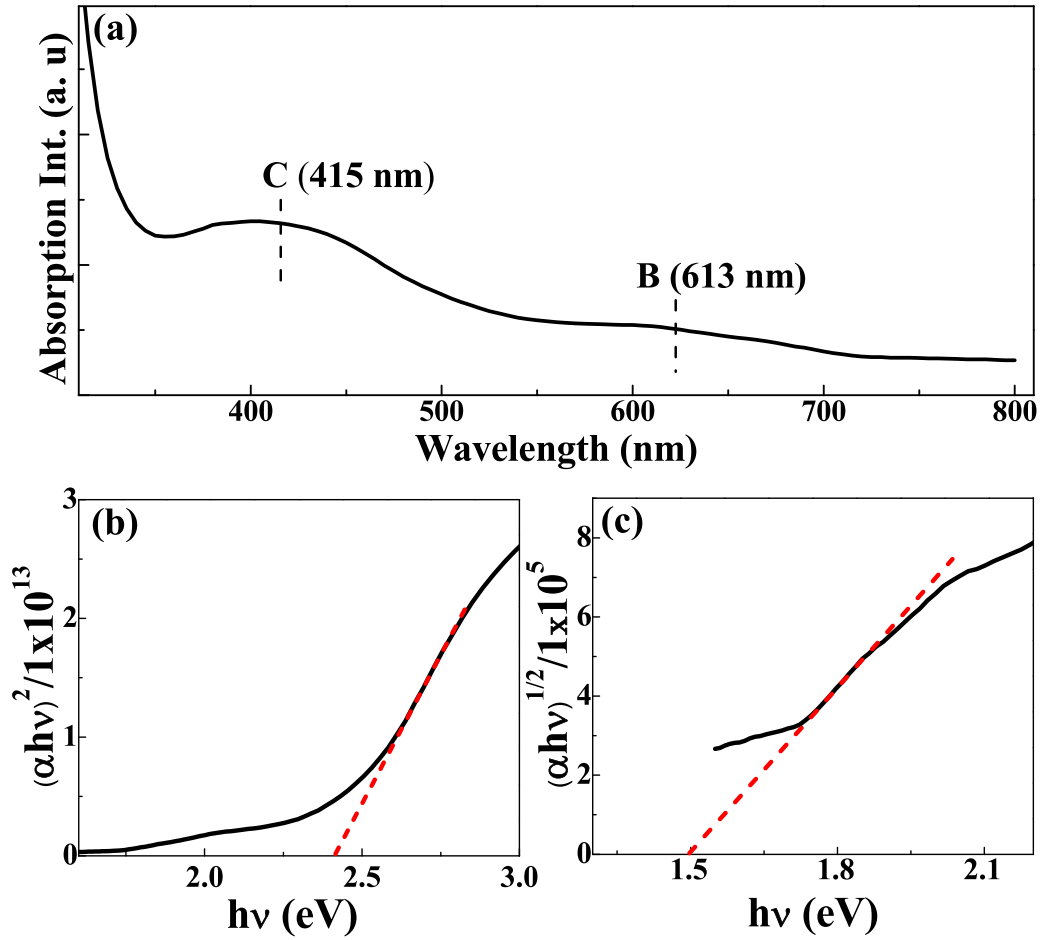


Figure 3. (a) Room temperature ($T = 300$ K) UV-Vis spectra of MoS₂ dendrite-like structure grown on glass. (b) Direct and (c) indirect Tauc plots of MoS₂. The dashed line in (b) and (c) is the linear fit to the linear portion of the Tauc plots.

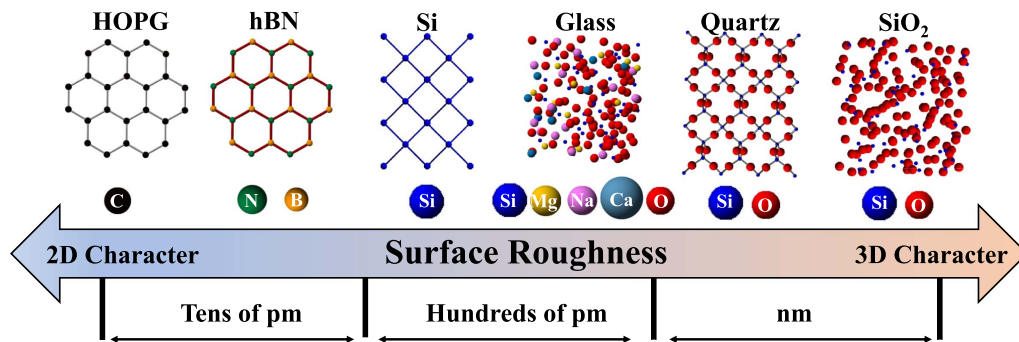


Figure 4. Schematic crystal structure of the growth substrates arranged in the order of their microscopic surface roughness.

of the aerosol particles and precursor decomposition thus leading to particle amalgamation with the formation of island-like growth. These dendrite-like structures have around 400 nm in thickness (see supporting information figure S6), with a vast number of nucleation sites on the SiO₂ surface. Similar shapes of growth were observed on the highly chemically reactive glass substrate even though its surface roughness is significantly smaller than quartz and SiO₂. This confirms chemical reactivity and surface roughness of the substrate play major roles in the morphology of MoS₂ growth. On the other hand,

the atomically smoother substrate of HOPG also provides dendrite-like structures at its grain boundaries and step edges.

Figure 5(a) shows the Raman spectra for the MoS₂ grown on different substrates. Raman spectroscopy further confirms the growth of 2H-MoS₂ by two active Raman modes at 383 cm⁻¹ and 408 cm⁻¹ which are assigned to the E_{2g}^1 and A_{1g} optical phonon modes, respectively [43, 51]. The Raman modes of MoS₂ grown on different substrates show blueshift with respect to the free-standing bulk MoS₂ crystal indicating substrate-induced strain [52–54]. Due to the bulk nature of the

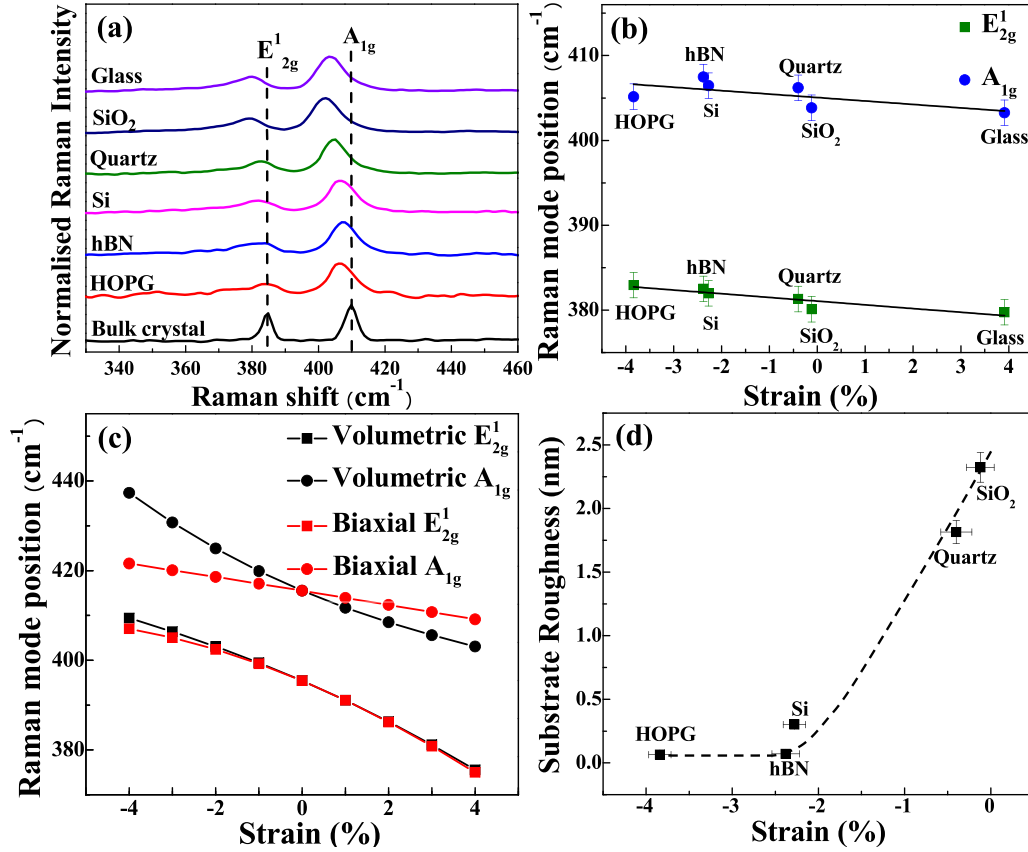


Figure 5. (a) Room temperature ($T = 300$ K) Raman spectra of MoS₂ grown on different substrates. Dependence of Raman mode positions on strain (b) experimental and (c) computational data. The straight lines in (b) are linear fits to data. (d) Compressive strain vs surface roughness of the substrates used for the MoS₂ growth. The dashed line in (d) is a guide to the eyes.

Table 1. Lattice parameters and corresponding strain of MoS₂ grown on different substrates.

Substrates used for MoS ₂ growth	In-plane lattice constant $a/\text{\AA}$	Out-of-plane lattice constant $c/\text{\AA}$	Strain/%	Crystal structure of the substrate and lattice mismatch with as-grown MoS ₂ /%
HOPG	3.04 ± 0.01	12.21 ± 0.01	-3.84 ± 0.13	Hexagonal, 28.45
Exfoliated hBN	3.08 ± 0.03	12.24 ± 0.05	-2.38 ± 0.16	Hexagonal, 26.19
Si	3.09 ± 0.01	12.15 ± 0.01	-2.27 ± 0.13	Cubic, 41.9
Z-Cut Quartz	3.15 ± 0.04	12.43 ± 0.07	-0.40 ± 0.18	Hexagonal, 36.79
SiO ₂	3.16 ± 0.03	12.06 ± 0.05	-0.12 ± 0.16	Amorphous structure
Glass	3.28 ± 0.01	12.43 ± 0.01	3.91 ± 0.13	Amorphous structure
Bulk MoS ₂	3.16 ± 0.01	12.25 ± 0.01	0.00	Hexagonal

grown films (thickness in the range of 100 nm–1.5 μm), this shift does not pertain to layer thickness dependence, which is commonly exerted for a few layers to monolayer MoS₂ [55]. Moreover, the A_{1g} mode did not show any peak splitting confirming this shift is not the result of charge doping as previously reported [56, 57]. One should note that the decrease in the ‘shoulder-like’ feature of the E_{2g}¹ mode alludes to the presence of fewer defects on the MoS₂ grown on SiO₂ and glass substrates, confirming the growth of high-quality MoS₂ [58].

The substrate-induced strain on the MoS₂ grown on different substrates was further examined by powder XRD. The MoS₂ characteristic planes of (002) and (004), respectively at $2\theta \approx 14^\circ$ and $\approx 28^\circ$ reconfirm the growth of hexagonal crystal structure (2H-phase) [43, 59], see supporting information figure S7. Table 1 shows the lattice constants and strain of MoS₂ grown on different substrates. The increase or decrease in the in-plane lattice constant of the as-grown MoS₂ with respect to the bulk MoS₂ crystal reconfirms the presence of substrate-induced strain. The substrate-induced

strain on MoS₂ grown on different substrates is calculated using the equation of, $\varepsilon = \frac{a_{(\text{as-grown})} - a_{(\text{bulk})}}{a_{(\text{bulk})}} \times 100\%$, where ε is strain and a is in-plane lattice constant. From table 1, one can note that the highly crystalline HOPG, exfoliated hBN, Si and quartz caused a lattice mismatch of >26% with the as-grown MoS₂. Moreover, these crystalline substrates induced compressive (negative) strain on the as-grown MoS₂. The amorphous glass induced tensile (positive) strain. However, the growth on the amorphous SiO₂ substrate appears to be least strained with near identical lattice constants compared to the bulk MoS₂ crystal.

To understand the dependence of Raman mode's peak position on substrate-induced strain, we compared our experimental results (figure 5(b)) with computational modelling (figure 5(c)). Density functional theory calculations [60, 61] were performed with local density approximation [61, 62] for the exchange-correlation functional and Quantum ESPRESSO package [63, 64]. Biaxial and volumetric strain for bulk MoS₂ was modelled using the lattice constants determined from XRD measurements. The comparison of experimental results with computational modelling confirms that the substrate-induced strain on the as-grown MoS₂ is biaxial (in-plane), not volumetric. Furthermore, we examined the calculated strain from XRD measurements with the substrate's surface roughness measured by AFM, which shows a correlation, see figure 5(d). The growth on smoother substrates exhibits higher degrees of compressive (positive) biaxial strain. With increasing surface roughness, the magnitude of compressive strain decreases. However, the MoS₂ grown on the glass substrate shows tensile (positive) biaxial strain, even though the surface roughness of glass is less than the quartz and SiO₂. This could be the combined result of the amorphous nature and the high chemical reactivity of the soda lime glass due to the presence of multiple atoms (Mg, Na, Si, Ca, and O) in its crystal structure.

4. Conclusion

In this study, we grew MoS₂ using a low-cost, low-temperature AACVD method and examined the role of substrate in the growth process. Through the alteration of the growth substrate, different degrees of biaxial strain can be induced to the MoS₂, which is studied by a combination of powder XRD, AFM, Raman spectroscopy, and computational methods. This study shows that the type of strain induced on the as-grown MoS₂ is a combined result of the substrate's surface roughness, crystallinity, and chemical reactivity. Crystalline substrates are favored for compressive strain and amorphous substrates induce almost negligible compressive strain (SiO₂) or tensile strain (glass). On the other hand, the magnitude of compressive strain decreases with increasing surface roughness. The as-grown MoS₂ shows the presence of direct and indirect bandgaps, the potential merit for photocatalytic and wavelength-tunable optoelectronic applications. The results of this study demonstrate that the AACVD is a viable method for high-quality MoS₂ production. This method could reduce the

material cost to fabricate next-generation electronic and optoelectronic devices.

Data availability statement

The data that support the findings of this study are openly available at the following URL/DOI: <https://doi.org/10.21252/c1by-d167>.

Acknowledgments

This work was supported by the Keele University, Royal Society [under Grants RSG/R2/212359, and SIF/R2/212004], Engineering and Physical Sciences Research Council (EPSRC) [under Grant EP/V043412/1], the UK Government and the European Union [under SEND programme 32R16P00706]. The authors acknowledge the Royce Equipment Access Scheme (under EPSRC Grant EP/R00661X/1) for the use of XPS and Dr Ben Spencer for technical support. The authors also thank Park Systems Ltd for AFM access and Dr James Kerfoot for technical support. L J A acknowledges Max Rimmer from the University of Manchester for his support during the access of the HITACHI TM4000Plus Tabletop Microscope for SEM and EDX studies at the National Graphene Institute.

Conflict of interest

The authors declare no conflicts of interest.

Authors contributions

N B and P D M designed the project. L J A grew the MoS₂ on different substrates and characterized them. J M M performed computational modelling. N B and L J A co-wrote the paper. All authors took part in the discussion and analysis of the data.

ORCID iDs

Lewis J Adams  <https://orcid.org/0009-0003-7497-2179>
 Peter D Matthews  <https://orcid.org/0000-0002-1362-8003>
 Juliana M Morbec  <https://orcid.org/0000-0002-1672-3575>
 Nilanthy Balakrishnan  <https://orcid.org/0000-0002-7236-5477>

References

- [1] Liu Y and Gu F 2021 A wafer-scale synthesis of monolayer MoS₂ and their field-effect transistors toward practical applications *Nanoscale Adv.* **3** 2117–38
- [2] Hua Q et al 2020 Atomic threshold-switching enabled MoS₂ transistors towards ultralow-power electronics *Nat. Commun.* **11** 1
- [3] Splendiani A, Sun L, Zhang Y, Li T, Kim J, Chim C Y, Galli G and Wang F 2010 Emerging photoluminescence in monolayer MoS₂ *Nano Lett.* **10** 1271–5

- [4] Radisavljevic B, Radenovic A, Brivio J, Giacometti V and Kis A 2011 Single-layer MoS₂ transistors *Nat. Nanotechnol.* **6** 147–50
- [5] Sanikop R and Sudakar C 2020 Tailoring magnetically active defect sites in MoS₂ nanosheets for spintronics applications *ACS Appl. Nano Mater.* **3** 576–87
- [6] Samy O, Zeng S, Birowosuto M D and Moutaouakil A E 2021 A review on MoS₂ properties, synthesis, sensing applications and challenges *Crystals* **11** 4
- [7] Matthews P D, McNaughton P D, Lewis D J and O'Brien P 2017 Shining a light on transition metal chalcogenides for sustainable photovoltaics *Chem. Sci.* **8** 4177–87
- [8] Liu M, Zhu H, Wang Y, Sevcenkan C and Li B L 2021 Functionalized MoS₂ -based nanomaterials for cancer phototherapy and other biomedical applications *ACS Mater. Lett.* **3** 462–96
- [9] Sun W, Zhang Y, Kang W, Deng N, Wang X, Kang X, Yan Z, Pan Y and Ni J 2022 Synthesis of MoS₂-based nanostructures and their applications in rechargeable ion batteries, catalysts and gas sensors: a review *RSC Adv.* **12** 19512–27
- [10] Chaves A et al 2020 Bandgap engineering of two-dimensional semiconductor materials *npj 2D Mater. Appl.* **4** 29
- [11] Jin W et al 2013 Direct measurement of the thickness-dependent electronic band structure of MoS₂ using angle-resolved photoemission spectroscopy *Phys. Rev. Lett.* **111** 106801
- [12] Zhu J, Wu J, Sun Y, Huang J, Xia Y, Wang H, Wang H, Wang Y, Yi Q and Zou G 2016 Thickness-dependent bandgap tunable molybdenum disulfide films for optoelectronics *RSC Adv.* **6** 110604–9
- [13] Lee H S, Min S-W, Chang Y-G, Park M K, Nam T, Kim H, Kim J H, Ryu S and Im S 2012 MoS₂ nanosheet phototransistors with thickness-modulated optical energy gap *Nano Lett.* **12** 3695–700
- [14] Bolar S, Shit S, Murmu N C, Samanta P and Kuila T 2021 Activation strategy of MoS₂ as HER electrocatalyst through doping-induced lattice strain, band gap engineering, and active crystal plane design *ACS Appl. Mater. Interfaces* **13** 765–80
- [15] Gong Y et al 2014 Band gap engineering and layer-by-layer mapping of selenium-doped molybdenum disulfide *Nano Lett.* **14** 442–9
- [16] He W, Shi J, Zhao H, Wang H, Liu X and Shi X 2020 Bandgap engineering of few-layered MoS₂ with low concentrations of S vacancies *RSC Adv.* **10** 15702–6
- [17] Jin K, Xie L, Tian Y and Liu D 2016 Au-modified monolayer MoS₂ sensor for DNA detection *J. Phys. Chem. C* **120** 11204–9
- [18] Rostami H, Roldán R, Cappelluti E, Asgari R and Guinea F 2015 Theory of strain in single-layer transition metal dichalcogenides *Phys. Rev. B* **92** 19
- [19] Manzeli S, Allain A, Ghadimi A and Kis A 2015 Piezoresistivity and strain-induced band gap tuning in atomically thin MoS₂ *Nano Lett.* **15** 5330–5
- [20] Castellanos-Gomez A, Roldán R, Cappelluti E, Buscema M, Guinea F, Van Der Zant H S J and Steele G A 2013 Local strain engineering in atomically thin MoS₂ *Nano Lett.* **13** 5361–6
- [21] Basu N, Kumar R, Manikandan D, Ghosh Dastidar M, Hedge P, Nayak P K and Bhallamudi V P 2023 Strain relaxation in monolayer MoS₂ over flexible substrate *RSC Adv.* **13** 16241–7
- [22] Carrascoso F, Li H, Frisenda R and Castellanos-Gomez A 2021 Strain engineering in single-, Bi- and Tri-Layer MoS₂, MoSe₂, WS₂ and WSe₂ *Nano Res.* **14** 1698–703
- [23] Datye I M, Daus A, Grady R W, Brenner K, Vaziri S and Pop E 2022 Strain-enhanced mobility of monolayer MoS₂ *Nano Lett.* **22** 8052–9
- [24] Yang S, Chen Y and Jiang C 2021 Strain engineering of TWO-DIMENSIONAL materials: methods, properties, and applications *InfoMat* **3** 397–420
- [25] Xia Y, Davis R S and Haataja M P 2019 Strain relaxation in misfitting transition metal dichalcogenide monolayer superlattices: wrinkling vs misfit dislocation formation *Nano Lett.* **19** 8724–31
- [26] Ponnusamy K, Durairaj S and Chandramohan S 2022 Effect of growth temperature on the morphology control and optical behavior of monolayer MoS₂ on SiO₂ substrate *J. Mater. Sci., Mater. Electron.* **33** 9549–57
- [27] Kim H, Ovchinnikov D, Deiana D, Unuchek D and Kis A 2017 Suppressing nucleation in metal-organic chemical vapor deposition of MoS₂ monolayers by alkali metal halides *Nano Lett.* **17** 5056–63
- [28] Bergeron H, Sangwan V K, McMorro J J, Campbell G P, Balla I, Liu X, Bedzyk M J, Marks T J and Hersam M C 2017 Chemical vapor deposition of monolayer MoS₂ directly on ultrathin Al₂O₃ for low-power electronics *Appl. Phys. Lett.* **110** 5
- [29] Liu X, Balla I, Bergeron H, Campbell G P, Bedzyk M J and Hersam M C 2016 Rotationally commensurate growth of MoS₂ on epitaxial graphene *ACS Nano* **10** 1067–75
- [30] Pollmann E, Madau L, Schumacher S, Kumar U, Heuvel F, Ende C V, Yilmaz S, Güngörmüş S and Schleberger M 2020 Apparent differences between single layer molybdenum disulfide fabricated via chemical vapour deposition and exfoliation *Nanotechnology* **31** 50
- [31] Plechinger G, Mann J, Preciado E, Barroso D, Nguyen A, Eroms J, Schüller C, Bartels L and Korn T 2014 A direct comparison of CVD-grown and exfoliated MoS₂ using optical spectroscopy *Semicond. Sci. Technol.* **29** 6
- [32] Savjani N, Brent J R and O'Brien P 2015 AACVD of molybdenum sulfide and oxide thin films from molybdenum (V)-based single-source precursors *Chem. Vapor Depos.* **21** 71–77
- [33] Lewis D J et al 2015 Thin films of molybdenum disulfide doped with chromium by aerosol-assisted chemical vapor deposition (AACVD) *Chem. Mater.* **27** 1367–74
- [34] Powell M J, Potter D B, Wilson R L, Darr J A, Parkin I P and Carmalt C J 2017 Scaling aerosol assisted chemical vapour deposition: exploring the relationship between growth rate and film properties *Mater. Des.* **129** 116–24
- [35] Dadgar A M, Scullion D, Kang K, Esposito D, Yang E H, Herman I P, Pimenta M A, Santos E J G and Pasupathy A N 2018 Strain engineering and Raman spectroscopy of monolayer transition metal dichalcogenides *Chem. Mater.* **30** 5148–55
- [36] Wang F, Kinloch I A, Wolverson D, Tenne R, Zak A, O'Connell E, Bangert U and Young R J 2017 Strain-induced phonon shifts in tungsten disulfide nanoplatelets and nanotubes *2D Mater.* **4** 1
- [37] Decoster M, Conan F, Guerchais J E, Mest Y L, Pala J S, Jeffery J C, Faulques E, Leblanc A and Molinie P 1995 Radical cation-radical anion salts: molybdenum complexes containing the [TCNQ]^{•+} or [TCNE]^{•+} radical anions x-ray crystal structure of [Mo(Et₂NCS₂)₄] (TCNQ) *Polyhedron* **14** 1741–50
- [38] Van der Aalsvoort J G M and Beurskens P T 1974 *Cryst. Struct. Commun.* **3** 653
- [39] Nawaz S, Khan Y, Khalid S, Malik M A and Siddiq M 2023 Molybdenum disulfide (MoS₂) along with graphene nanoplatelets (GNPs) utilized to enhance the capacitance of conducting polymers (PANI and PPy) *RSC Adv.* **13** 28785–97
- [40] Li Y, Kuang G, Jiao Z, Yao L and Duan R 2022 Recent progress on the mechanical exfoliation of 2D transition metal dichalcogenides *Mater. Res. Express* **9** 122001

- [41] McCain M N, He B, Sanati J, Wang Q J and Marks T J 2008 Aerosol-assisted chemical vapor deposition of lubricating MoS₂ films. Ferrous substrates and titanium film doping *Chem. Mater.* **20** 5438–43
- [42] Fairley N CasaXPS 2019 (available at: www.casaxps.com)
- [43] Zeng N, Hopkinson D G, Spencer B F, McAdams S G, Tedstone A A, Haigh S J and Lewis D J 2019 Direct synthesis of MoS₂ or MoO₃ via thermolysis of a dialkyl dithiocarbamate molybdenum (iv) complex *Chem. Commun.* **55** 99–102
- [44] Li Y, Chang K, Sun Z, Shangguan E, Tang H, Li B, Sun J and Chang Z 2020 Selective preparation of 1T- and 2H-phase MoS₂ nanosheets with abundant monolayer structure and their applications in energy storage devices *ACS Appl. Energy Mater.* **3** 998–1009
- [45] Salehi N and Abareshi A 2022 Study of structural, optical, and thermal properties in MoS₂-based nanocomposites: iron and gold *Eur. Phys. J. Plus* **137** 11
- [46] Saha N, Sarkar A, Ghosh A B, Dutta A K, Bhadu G R, Paul P and Adhikary B 2015 Highly active spherical amorphous MoS₂: facile synthesis and application in photocatalytic degradation of rose bengal dye and hydrogenation of nitroarenes *RSC Adv.* **5** 88848–56
- [47] Ehsan M A, Ming H N, Misran M, Arifin Z, Tiekink E R T, Safwan A P, Ebadi M, Basirun W J and Mazhar M 2012 Effect of AACVD processing parameters on the growth of greenockite (CdS) thin films using a single-source cadmium precursor *Chem. Vapor Depos.* **18** 191–200
- [48] Chae W H, Cain J D, Hanson E D, Murthy A A and Dravid V P 2017 Substrate-induced strain and charge doping in CVD-grown monolayer MoS₂ *Appl. Phys. Lett.* **111** 14
- [49] Lei Y et al 2021 Low temperature activation of inert hexagonal boron nitride for metal deposition and single atom catalysis *Mater. Today* **51** 108–16
- [50] Moritz D C, Calvet W, Zare Pour M A, Paszuk A, Mayer T, Hannappel T, Hofmann J P and Jaegermann W 2023 Dangling bond defects on Si surfaces and their consequences on energy band diagrams: from a photoelectrochemical perspective *Solar RRL* **7** 2201063
- [51] Li H, Zhang Q, Yap C C R, Tay B K, Edwin T H T, Olivier A and Baillargeat D 2012 From bulk to monolayer MoS₂: evolution of Raman scattering *Adv. Funct. Mater.* **22** 1385–90
- [52] Yang L, Cui X, Zhang J, Wang K, Shen M, Zeng S, Dayeh S A, Feng L and Xiang B 2014 Lattice strain effects on the optical properties of MoS₂ nanosheets *Sci. Rep.* **4** 5649
- [53] Pradhan G and Sharma A K 2018 Anomalous Raman and photoluminescence blue shift in mono- and a few layered pulsed laser deposited MoS₂ thin films *Mater. Res. Bull.* **102** 406–11
- [54] Liu C W et al 2020 Substrate-induced strain in 2D layered GaSe materials grown by molecular beam epitaxy *Sci. Rep.* **10** 1
- [55] Ye M, Winslow D, Zhang D, Pandey R and Yap Y K 2015 Recent advancement on the optical properties of two-dimensional molybdenum disulfide (MoS₂) thin films *Photonics* **2** 288–307
- [56] Velický M et al 2020 Strain and charge doping fingerprints of the strong interaction between monolayer MoS₂ and gold *J. Phys. Chem. Lett.* **11** 6112–8
- [57] Rice C, Young R J, Zan R, Bangert U, Wolverson D, Georgiou T, Jalil R and Novoselov K S 2013 Raman-scattering measurements and first-principles calculations of strain-induced phonon shifts in monolayer MoS₂ *Phys. Rev. B* **87** 8
- [58] Mignuzzi S, Pollard A J, Bonini N, Brennan B, Gilmore I S, Pimenta M A, Richards D and Roy D 2015 Effect of disorder on raman scattering of single-layer MoS₂ *Phys. Rev. B* **91** 19
- [59] Schneemeyer L F and Sienko M J 1980 Crystal data for mixed-anion molybdenum dichalcogenides *Inorg. Chem.* **19** 789–91
- [60] Kohn W 1999 Nobel lecture: electronic structure of matter—wave functions and density functionals *Rev. Mod. Phys.* **71** 1253–66
- [61] Kohn W and Sham L J 1965 Self-consistent equations including exchange and correlation effects *Phys. Rev.* **140** A1133–8
- [62] Perdew J P and Zunger A 1981 Self-interaction correction to density-functional approximations for many-electron systems *Phys. Rev. B* **23** 5048–79
- [63] Giannozzi P et al 2009 QUANTUM ESPRESSO: a modular and open-source software project for quantum simulations of materials *J. Phys.: Condens. Matter* **21** 395502
- [64] Giannozzi P et al 2017 Advanced capabilities for materials modelling with quantum ESPRESSO *J. Phys.: Condens. Matter* **29** 465901